Chemical Engineering Journal 451 (2023) 139013

Contents lists available at ScienceDirect

Chemical Engineering Journal

journal homepage: www.elsevier.com/locate/cej

Construction of strongly coupled few-layer $FePSe_3$-CNT hybrids for high performance potassium-ion storage devices

Yan-Fu Huang, Yi-Chun Yang, Hsing-Yu Tuan *

Department of Chemical Engineering, National Tsing Hua University, Hsinchu 30013, Taiwan

ARTICLE INFO

Keywords:
Ternary metal phosphorus trichalcogenides
Potassium-ion batteries
Potassium-ion hybrid capacitor
1D-2D hybrids
Layered material

ABSTRACT

Given the layered crystal structure and tunable composition, ternary metal phosphorus trichalcogenides ($MPCh_3$) is an attractive anode material for potassium-ion batteries with higher surface activity and mobility than their binary analogues. However, how to improve the electronic conductivity, ion diffusion, and maintain high reversible potassiation/depotassiation processes are the main key issues for the development of $MPCh_3$-based electrodes with high rate and long cycle life. For example, theoretically, $FePSe_3$ has a layered crystal structure with high electronic conductivity and low diffusion barrier, yet their K^+-based electrochemical performance not well demonstrated. Here, we report a mechanical exfoliation method to prepare few-layer $FePSe_3$-carbon nanotube (f-$FePSe_3$/CNT) hybrids for use as high-efficiency K^+ storage anodes. Electrochemical performance, kinetic analysis, reaction mechanism analysis, and density functional theory calculations show that this strongly coupled 1D-2D hybrids promotes the reaction and diffusion of potassium ions, giving full play to the inherent advantages of materials with different dimensions. Therefore, the f-$FePSe_3$/CNT PIB anodes exhibit high capacity (472.1 mA h g^{-1}, 0.05 A/g), high rate (124.9 mA h g^{-1}, 10 A/g), and cycling stability (>1000 cycles), which significantly exceeds the performance of its binary analogue, here FeSe. In addition, the full cells of potassium-ion battery and hybrid capacitor coupled with f-$FePSe_3$/CNT anodes exhibit good cycling stability (500 cycles) and high energy/power density of 54.7 W h kg^{-1}/5790.8 W kg^{-1}, respectively, revealing its practical applications in a wide range of K^+-based storage systems. We believe that this work will provide a universal strategy for effectively activating the K^+ electrochemical performance on a wide range of layered materials.

1. Introduction

Potassium-ion batteries (PIBs) have been developed to provide an alternative to lithium-ion batteries based on more abundant and low-cost materials [1–3]. However, the large ionic radius of K^+ leads to poor cycling performance and rate capability due to large volume change and slow redox kinetics during cycling [4–6]. Graphite is the traditional lithium-ion batteries anode, yet the challenge of using graphite as a PIB anode is limited cycle stability far behind Li-ion batteries and low theoretical capacity (KC_8; 279 mA h g^{-1}) [7–10]. Recently, two-dimensional (2D) few-layer sheets via exfoliation of layered materials has attracted great interest as a new candidate for energy storage applications due to their fascinating electronic and physicochemical properties [11,12]. 2D materials are special materials with atomic-thick layered structures that are bound together by strong covalent or ionic bonds and stacked together by weak van der Waals forces [13]. Two main characteristics of 2D materials make it an interesting energy storage material: (1) The large surface area of 2D materials is beneficial to ion adsorption and improved capacitance [14]. (2) The high electrical conductivity of 2D materials and tunable interlayer spacing can facilitate electron transfer and ion intercalation [15–17].

Recently, ternary 2D metal phosphorus trichalcogenides ($MPCh_3$, where M = V, Mn, Fe, Co, Ni, Zn, etc. and Ch = S, Se) is expected to become a new generation of energy storage materials. Compared to 2D carbon materials (e.g., graphene [18] and MXenes [19]) or binary materials (e.g., MoS_2 [20], SnS_2 [21], VSe_2 [4] and WSe_2 [22], etc.), $MPCh_3$ layers with metal cations and $[P_2S_6]^{4-}$ or $[P_2Se_6]^{4-}$ anions are held through van der Waals force, leading to unique structure, tunable composition, high surface activity and high mobility [23–25]. The excitonic insulating phase, intrinsic ferromagnetism, and high electron mobility of ternary metal phosphorus chalcogenides has higher electrical conductivity and tunable electronic states compared with the corresponding metal phosphides and sulfides. In particular, Feng *et al.*

* Corresponding author.
E-mail address: hytuan@che.nthu.edu.tw (H.-Y. Tuan).

https://doi.org/10.1016/j.cej.2022.139013
Received 30 June 2022; Received in revised form 26 August 2022; Accepted 1 September 2022
Available online 5 September 2022

found that the Na-ion full cell with CoPSe/NC anode can achieve an energy density of 274 Wh kg^{-1}, which is better than that of the binary $CoSe_2$/NC full cells [26]. In principle, van der Waals bonded layered compounds through mechanical exfoliation techniques can produce a single or few layer, thus increasing the electrochemical specific surface area and interlayer spacing to facilitate ion/electron transport [27,28]. Often, the reduction of material thickness to a single layer or a few layers results in unique and potentially useful electronic properties [29]. For example, the electronic structure of the 2D material MoS_2 changes from an indirect gap to a direct gap with decreasing size, and the band gap of single layer MoS_2 is wider than that of 3D bulk MoS_2 [30,31]. Hao *et al.* reported $FePSe_3$ nanosheets with controlled oxygen doping for zinc-air batteries, which exhibited high round-trip efficiency (60.65 %) and long-term stability (280 h) [32]. Sang *et al.* prepared a 2D/2D hybrid of $MnPS_3$/rGO with the specific capacity of 315 mA h g^{-1} at 0.2 A/g, indicating its excellent performance in sodium-ion battery [33].

However, for large scale exfoliation, ball milling or liquid phase exfoliation methods sometimes result in impurities and defects, which would have non-negligible effects on their properties. Therefore, the strategy of mixing different dimensions materials can reduce the agglomeration caused by exfoliation to improve the conductivity and surface area of the composites [34]. Combining material of different dimensions can inherit the original advantages of materials in each dimension, such as 1D-2D composite materials [35,36]. 1D nanotubes have large specific surface area and good stability, while 2D materials have abundant active sites [37]. For the 1D-2D structure, the agglomeration of 2D materials can be improved, and it has excellent electrical conductivity, making its hybrids useful for improved electrochemical performance of batteries. For example, Ye *et al.* reported that a 1D-2D MXene-CoTe modified separator improves electrolyte wettability and Li-ion transport, so that Li-S batteries achieve excellent rate capability, and long-life cyclability [38]. Luo *et al.* reported that 1D-2D $Na_3Ti_5O_{12}$-MXene hybrid anode exhibits stable cycling performance even under 10 mA cm^{-2} for sodium ion batteries [39]. Despite this extraordinary electrochemical performance of 1D-2D hybrid, it is critical that the interfacial coupling strength is not controlled. Traditionally, 1D-2D hybrid structures can be obtained by self-assembly or layer-by-layer assembly, and the synthesis process is relatively complicated [39]. Unfortunately, the interaction area between the 1D and 2D materials is very small, which is susceptible to other molecules. Therefore, a new strategy needs to be explored to produce 1D-2D hybrids with strong coupling interaction.

In this work, we explore an efficient strategy to synthesize strongly coupled f-$FePSe_3$-CNT hybrids as anodes for PIBs. The special architecture of 2D f-$FePSe_3$ tightly wound with carbon nanotubes can enhance electronic conductivity, promote K^+ diffusion, and effectively reduce the aggregation of f-$FePSe_3$ and the buffer volume change. Importantly, it can effectively activate the high performance of $FePSe_3$ PIB anodes, making them promising PIB anode materials.

2. Experimental section

2.1. Synthesis of $FePSe_3$

$FePSe_3$ was synthesized by a vacuum solid-state method, which was slightly modified from previous research [40]. The iron powder (J.T. Baker), red phosphorous powder (Sigma-Aldrich, 97 %) and selenium powder (Sigma-Aldrich, 99.99 %) (the molar ratio is 1:1:3) were loaded into a vacuum quartz tube. The tube was sealed and then placed in furnace. The temperature was kept at 700 °C for 24 h. After completion of reaction and natural cooling to room temperature, the quartz tube was broken using a diamond cutter and samples were collected.

2.2. Synthesis of f-$FePSe_3$

The f-$FePSe_3$ was synthesized by wet milling method. The samples were prepared by mixing 90 mg of $FePSe_3$ and 1 mL of 2-propanol (J.T. Baker, ≥99.5 %). The mixture was placed into a stainless-steel jar (12 cm^3) with stainless-steel balls (diameter of 3/8 in.) in a planetary ball mill (PM 100, RETSCH) at a rotation speed of 230 rpm for 20 h.

2.3. Synthesis of f-$FePSe_3$/CNT and f-$FePSe_3$/graphite

The f-$FePSe_3$/CNT composites were synthesized via high energy mechanical milling (HEMM). $FePSe_3$ and multi-walled carbon nanotube (the mass ratio was 2:1) were placed into a stainless-steel jar with stainless-steel balls and sealed inside an argon-filled glovebox. The mass ratio of ball to powder is about 180:1. Finally, the mixture was ball milled for 24 h. The f-$FePSe_3$/graphite was prepared by a similar procedure with adding graphite instead of CNT.

2.4. Synthesis of few-layer FeSe (f-FeSe) and f-FeSe/CNT

The f-FeSe were prepared by a one-step hydrothermal method, which was slightly modified from previous research [41]. In a typical synthesis, 0.099 g of $FeCl_2{\cdot}4H_2O$ (Alfa Aesar, 98 %), 0.055 g of SeO_2 (Alfa Aesar, 99.4 %), 0.2 g of NaOH, and 0.03 g polyvinyl pyrrolidone (PVP, Sigma-Aldrich, M.W. ~ 55,000) were dissolved under vigorous magnetic stirring in 10.0 mL of glycol (Sigma-Aldrich, 98 %) for 2 h. The mixture was sealed in a Teflon-lined stainless steel autoclave (50 mL) and maintained at 220 °C for 12 h. Followed by natural cooling to ambient temperature, the resulted solid products were collected by centrifugation and washed with DI water and ethanol twice. In order to prepare f-FeSe/CNT, the synthesis conditions are the same as f-$FePSe_3$/CNT.

2.5. Material and electrochemical characterization

The microstructure and electrochemical performance of the as-prepared samples ($FePSe_3$, f-$FePSe_3$, f-$FePSe_3$/CNT, f-$FePSe_3$/graphite, f-FeSe and f-FeSe/CNT) were tested by a series of experiment. The details of equipment and experiment are described in the Supporting Information.

2.6. Computational method

Our calculations were performed by means of density functional theory (DFT) using the Vienna Ab-initio Simulation Package (VASP). The details of DFT calculation is provided in the Supporting Information.

3. Results and discussion

The synthetic process of f-$FePSe_3$/CNT hybrids is shown in Fig. 1a. A layered crystalline material was obtained by a vacuum solid-state method. First, the high-purity elements of Fe, P and Se were sealed in the vacuum quartz tube. Then, the layered crystal $FePSe_3$ products were finally collected after the tube was placed in furnace at 700 °C for 24 h. Next, in order to obtain f-$FePSe_3$/CNT hybrids, the layered $FePSe_3$ and CNTs were uniformly mixed by ball milling at 180 rpm. During the synthesis process, the strong interaction between the layered structure of $FePSe_3$ and the steel balls physically exfoliates $FePSe_3$. Mechanical pathways (normal and shear forces) can overcome the attractive force and van der Waals resistance between $FePSe_3$ layers, so that the layered structure of $FePSe_3$ can be exfoliated layer by layer to form small and thin f-$FePSe_3$. Among them, CNTs are interleaved between $FePSe_3$ layers to form 3D f-$FePSe_3$/CNT composites. This hybrid composites usually exhibit unique synergistic effects, and the introduction of conductive materials into 2D materials can effectively overcome the inherent problems of low conductivity and large volume change of raw materials, making these 2D materials in electrochemical more attractive. Therefore, the entangled 1D CNTs provide a 3D scaffold for $FePSe_3$ due to good flexibility, stability, and high electrical conductivity, thereby optimizing the electrochemical performance of $FePSe_3$ and satisfying the

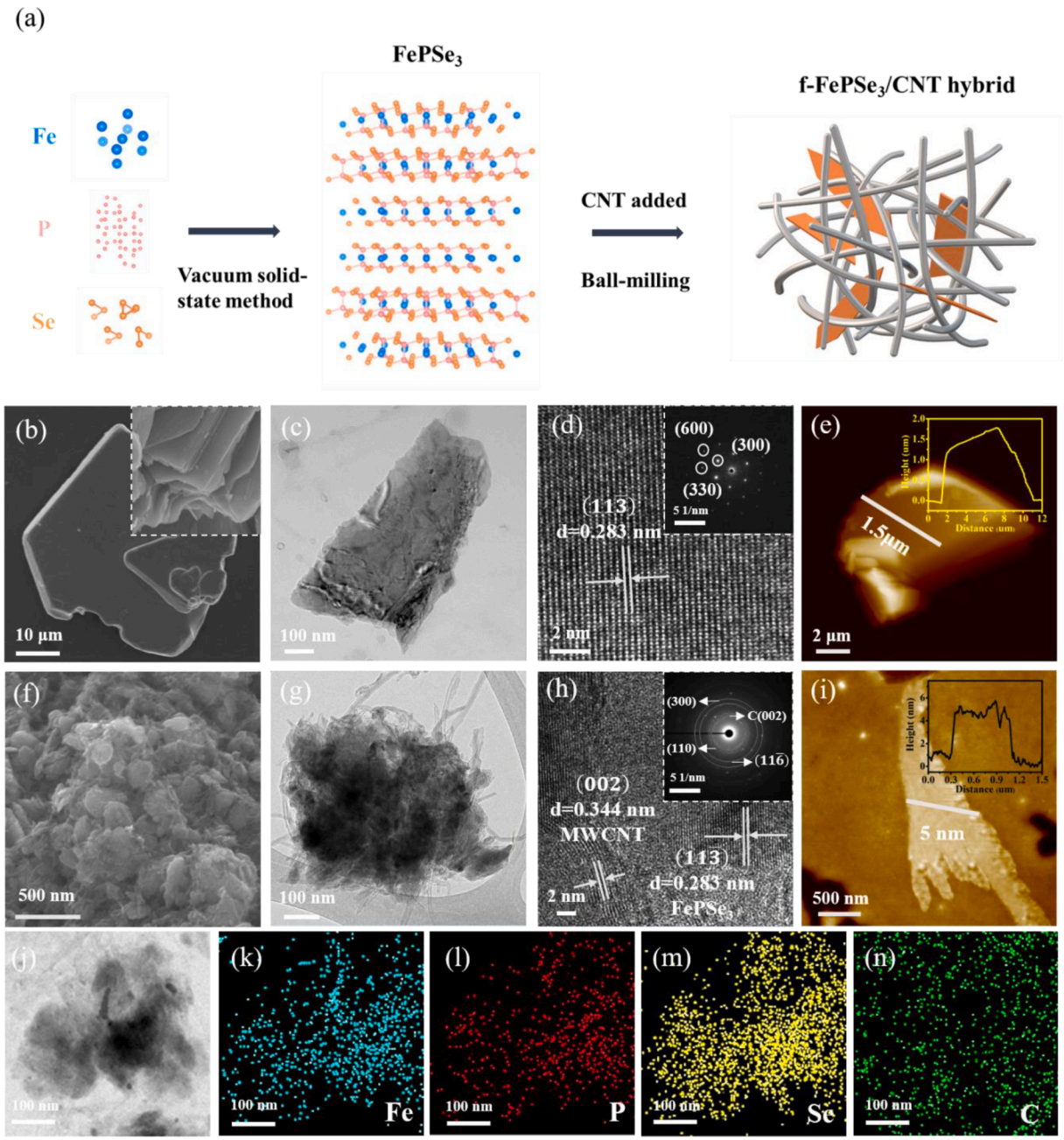

Fig. 1. (a) Schematic of the synthesis process of 2D/1D f-$FePSe_3$/CNT hybrid. SEM, TEM, HRTEM, and AFM images of (b–e) $FePSe_3$ and (f–i) f-$FePSe_3$/CNT. Inset of (d) and (h) is SAED pattern of $FePSe_3$ and f-$FePSe_3$/CNT. (j–n) EDS elements mappings of f-$FePSe_3$/CNT.

potassium ion storage requirement. The scanning electron microscope (SEM) and transmission electron microscope (TEM) images of the as-synthesized $FePSe_3$ clearly show the typical stacked layered structure (Fig. 1b and c). The microstructure of $FePSe_3$ was further observed by high-resolution transmission electron microscopy (HRTEM), selected area electron diffraction (SAED), and atomic force microscopy (AFM) (Fig. 1d and e). In Fig. 1d, the layered structure of $FePSe_3$ with a d-spacing of 0.238 nm can be clearly observed, corresponding to the (1 1 $\bar{3}$) plane of $FePSe_3$ (PDF #04–007-2803). Furthermore, the SAED pattern shows regular rhombohedral spots, confirming the single-crystal structure of $FePSe_3$ (Fig. 1d inset). The thickness of the layered $FePSe_3$ is about 1.5 μm as measured by the height profile by AFM (Fig. 1e). The elemental composition measured by scanning TEM energy dispersive spectroscopy (STEM-EDS) element mapping analysis indicates that the as-prepared $FePSe_3$ is uniformly composed of Fe, P and Se elements (Figure S1). Fig. 1f and g show the microstructure of f-$FePSe_3$/CNT hybrids analyzed by SEM and TEM. It can be found that the CNTs are closely intertwined with the f-$FePSe_3$, which indicates that the original layered structure of $FePSe_3$ can be successfully exfoliated into a f-$FePSe_3$ through the ball milling method, and the CNTs are uniformly wound around the f-$FePSe_3$. Notably, except for some structural damage during ball milling, the tubular structure of CNTs can be clearly observed in the SEM images. CNTs as framework embedded in the $FePSe_3$ layers can enhance mechanical stability, improve electrical conductivity, and reduce $FePSe_3$ restacking. Fig. 1h shows the HRTEM image of the f-$FePSe_3$/CNT composite and the lattice fringes with a d-spacing of 0.283 nm belong to the (1 1 $\bar{3}$) plane of the pristine $FePSe_3$. Furthermore, the lattice fringes with a d-spacing of 0.344 nm corresponds to the (0 0 2) lattice plane of the CNTs, demonstrating that f-$FePSe_3$ is successfully distributed in the CNTs. The SAED pattern of f-$FePSe_3$/CNT is shown in

the inset. The SAED pattern can point to the (1 1 0), (1 1 $\bar{6}$), and (3 0 0) planes of $FePSe_3$ and the (0 0 2) plane of CNT. In addition, the height of f-$FePSe_3$ after exfoliated is analyzed through AFM measurement, as shown in Fig. 1i. The thickness of f-$FePSe_3$ is about 5 nm. And, the morphology of f-$FePSe_3$ and binary analogue (f-FeSe) is shown in Figure S2. The STEM-EDS element mapping results show that the as-prepared f-$FePSe_3$/CNT is uniformly composed of Fe, P, Se and C elements (Fig. 1j–n). In addition, the detailed microstructures of f-FeSe after mixing with CNT are also explored by SEM, TEM, SAED, HRTEM, and EDS showing that CNTs are uniformly wound around FeSe (Figure S3).

The X-ray diffraction (XRD) patterns of $FePSe_3$, f-$FePSe_3$, and f-$FePSe_3$/CNT are shown in Fig. 2a. All of XRD peaks are consistent with $FePSe_3$, confirming that the crystalline structure of $FePSe_3$ is not changed after ball milling. Meanwhile, an extra peak at 26.4° in the XRD patterns of f-$FePSe_3$/CNT can be observed, which can be attributed to the (0 0 2) plane of CNT. Moreover, the XRD patterns of f-FeSe and f-FeSe/CNT show that both of XRD peaks are consistent with FeSe (Figure S4). The Raman spectra of $FePSe_3$, f-$FePSe_3$/CNT and f-FeSe/CNT are shown in Fig. 2b. The Raman spectrum has two peaks at 1340 cm^{-1} (D-band) and 1580 cm^{-1} (G-band), corresponding to disordered and ordered carbons, respectively. The peak intensity ratio of the D band to the G band reflects the disorder degree of the carbon material [42,43]. The D/G intensity ratio of f-$FePSe_3$/CNT and f-FeSe/CNT indicates an increase the defects, properties that can improve electrical conductivity and facilitate reaction kinetics [44]. The carbon content of f-$FePSe_3$/CNT is approximately 33 % by thermogravimetric analysis (TGA) (Figure S5). The current–voltage (I-V) curves of $FePSe_3$ and f-$FePSe_3$/CNT are shown in Fig. 2c. Based on the Ohm's law: $V = I \times R$, the fit line curve of current (i) and voltage (V) can determine the slope (R, resistance). And, according to law of resistance: $R = \rho\frac{L}{A}$, the resistance is the ratio of the thickness (L) and cross-section area (A) of the electrode multiplied by the resistivity (ρ). Therefore, the conductivity (σ) can be calculated: $= \frac{1}{\rho}$. Fig. 2d shows that the conductivity of f-$FePSe_3$/CNT (0.132 S m^{-1}) is about 10^5 times as high as $FePSe_3$ (9.764 × 10^{-6} S m^{-1}), suggesting that the conductivity of $FePSe_3$ can be effectively increased after mixing with CNTs [45]. The C, Fe, P, and Se compositions of f-$FePSe_3$/CNT and $FePSe_3$ were analyzed by X-ray photoelectron spectroscopy (XPS) (Fig. 2e–h, S6 and S7). Fig. 2e can be deconvoluted into two peaks at 285.6 and 284.8 eV, assigned to C—O and C—C, respectively [46]. In Fig. 2f, the two peaks at around 711.2 and 724.7 eV belong to the $2p_{3/2}$ and $2p_{1/2}$ levels of Fe^{2+} while the other two strong peaks located at 714.5 and 728.7 eV, assigned to the $2p_{3/2}$ and $2p_{1/2}$ levels of Fe^{3+}, indicating the co-existence of both Fe^{2+} and Fe^{3+} in f-$FePSe_3$/CNT. In Fig. 2g, the peaks located at 131.9 and 133.2 eV, corresponding to P $2p_{3/2}$ and P $2p_{1/2}$ [32,47]. Additionally, the peak of PO_x at 134.4 eV can be observed due to surface oxidation of the samples exposed to the atmosphere after fabrication. In the Se 3d spectrum, the peaks located at 55.4 and 56.2 eV, assigned to Se $3d_{5/2}$ and Se $3d_{3/2}$, respectively (Fig. 2h) [48]. The probable chemical connection between f-$FePSe_3$ and CNTs was investigated by surface time-of-flight secondary ion mass spectrometry (ToF-SIMS). Fig. 2i shows clear peaks associated with Fe – O — C, P — C, P — O — C, Se – C, and Se – O — C bonds, respectively, confirming the formation of chemical bonds between f-$FePSe_3$ and CNTs during ball milling.

In order to explore the influence of 3D structure and the difference of $FePSe_3$ and FeSe on electrochemical performance. The difference between FeSe and $FePSe_3$ materials was initially observed through simulation calculations (Figure S8). Fig. 3a shows the CV curves of f-$FePSe_3$/CNT under 0.1 mV s^{-1}. During the initial cathodic process, a strong cathodic peak is obtained at about 1.45 V, which is attributed to the formation of the solid-electrolyte interphase (SEI) film and the insertion of K^+ into $FePSe_3$ to form Fe, P and K_2Se. Subsequently, another strong peak appears at 0.75 V, which is due to the reaction of K^+ with P to form K_4P_3. In the anodic process, an oxide peak at about 1.80 V can be attributed to the reversible reaction and the formation of $FePSe_3$. All

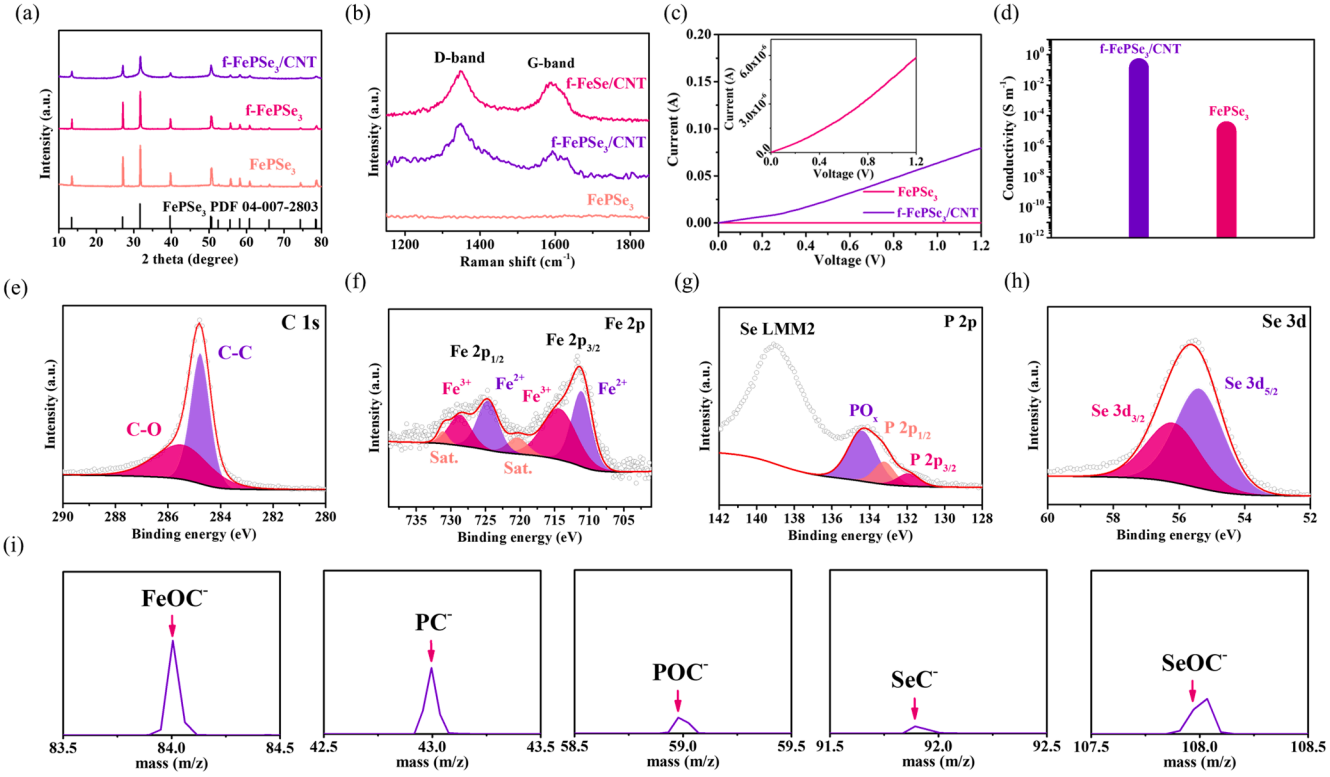

Fig. 2. (a) XRD patterns of $FePSe_3$, f-$FePSe_3$, and f-$FePSe_3$/CNT. (b) Raman spectra of $FePSe_3$, f-$FePSe_3$/CNT, and f-FeSe/CNT. (c) I – V curves of $FePSe_3$ and f-$FePSe_3$/CNT. The inset image is the I – V curve of $FePSe_3$, ranging from 0 – 10^{-5}A. (d) Comparison of conductivity of $FePSe_3$ and f-$FePSe_3$/CNT. (e–h) High-resolution C 1 s, Fe 2p, P 2p, and Se 3d XPS spectra of f-$FePSe_3$/CNT. (i) ToF-SIMS spectra of $FeOC^-$, PC^-, POC^-, SeC^-, and $SeOC^-$ fragments for f-$FePSe_3$/CNT.

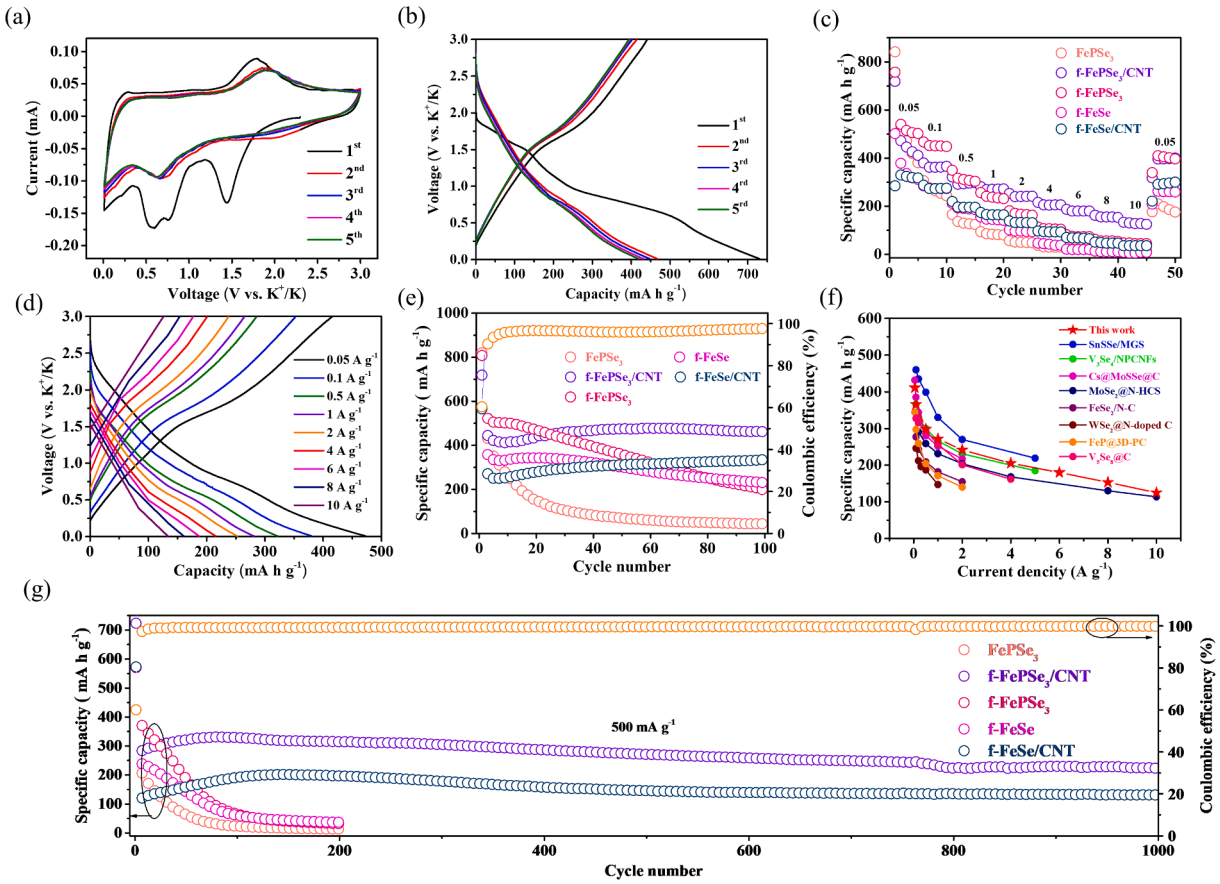

Fig. 3. (a) CV profiles at a scan rate of 0.1 mV s^{-1} and (b) galvanostatic charge/discharge curves at 50 mA g^{-1} for f-$FePSe_3$/CNT. (c) Rate performance of different electrodes at various current densities from 0.05 to 10 A/g. (d) Galvanostatic charge/discharge curves of f-$FePSe_3$/CNT at various current densities. (e) Cycling performance of different electrodes at a current density of 50 mA g^{-1}. (f) Rate performance comparison of f-$FePSe_3$/CNT with previously reported anode materials. (g) Long-term cycling performance of different electrodes at a current density of 500 mA g^{-1}.

peaks almost overlap after the second cycle, indicating highly reversible electrochemical performance. The CV curves of f-FeSe/CNT under 0.1 mV s^{-1} is shown in Figure S9. Additionally, the rate and cycling performance of the CNTs electrode were investigated. Figure S10 shows that pure CNTs cannot contribute to the capacity for the f-$FePSe_3$/CNT electrode. Fig. 3b shows the discharge–charge curves of f-$FePSe_3$/CNT for the first five cycles. The initial discharge/charge capacity of f-$FePSe_3$/CNT are 730.6 and 441.2 mA h g^{-1}, respectively, and the initial Coulombic efficiency (ICE) is about 60.39 %. The rate performance of $FePSe_3$, f-$FePSe_3$, f-$FePSe_3$/CNT, f-FeSe and f-FeSe/CNT was tested at different rates from 0.05 to 10.0 A g^{-1} in Fig. 3c. $FePSe_3$ only delivers the low capacity of 124.2 mA h g^{-1} at low rate of 0.5 A g^{-1}, and then the capacity almost declines to zero at high rate of 6 A g^{-1}, which can be attributed to the material fragmentation after K^+ intercalation. In addition, although the capacity of f-$FePSe_3$ is higher than that of $FePSe_3$, it also decays quickly after high rate of 6 A g^{-1}. The electrochemical performance of $FePSe_3$ is improved through the strategy of 1D/2D hybrid nanoarchitecture, f-$FePSe_3$/CNT electrode delivers the capacities of 472.1, 379.8, 321.6, 281.1, 252.7, 215.5, 186.6, 162.2, and 133.3 mA h g^{-1} at the current density of 0.05, 0.1, 0.5, 1, 2, 4, 6, 8, and 10 A g^{-1}, respectively (Fig. 3c). On the other hand, the strategy of 2D/2D hybrid (f-$FePSe_3$/graphite) was investigated. The detailed microstructures and characterization of f-$FePSe_3$/graphite were explored by SEM, TEM, SAED, HRTEM, EDS, XRD, Raman spectroscopy, TGA and XPS (Figures S11 and S12). The f-$FePSe_3$/graphite electrode delivers the capacities of462.9, 366.9, 305.9, 266.6, 235.5, 199.9, 178.3, 164.4 and 152.7 mA h g^{-1} at the current density of 0.05, 0.1, 0.5, 1, 2, 4, 6, 8, and 10 A g^{-1}, respectively (Figure S13). There is no particular difference between the 1D/2D hybrid and 2D/2D hybrid in the rate performance test. In addition, comparing the difference between $FePSe_3$ and FeSe, it can be clearly observed that the rate performance of f-FeSe/CNT is lower than that of f-$FePSe_3$/CNT. This result is consistent with the DFT result. The relatively low energy barrier facilitates fast ion diffusion and electrochemical reaction kinetics. Notably, the rate performance of FeSe is also improved after mixing with CNT, indicating that CNTs embedded in the layered materials can improve the rate performance. Fig. 3d shows the charge–discharge curves of f-$FePSe_3$/CNT at different rates. The cycling performance of $FePSe_3$, f-$FePSe_3$, f-$FePSe_3$/CNT, f-FeSe and f-FeSe/CNT was evaluated at 0.05 A g^{-1} (Fig. 3e). First of all, the capacity of $FePSe_3$ has an obvious downward trend before 20 cycles, but the cycle performance of f-$FePSe_3$ and f-$FePSe_3$/CNT is significantly improved. The f-$FePSe_3$/CNT delivers the capacity of 461.6 mA h g^{-1} after 100 cycles, whereas f-$FePSe_3$ has an obvious downward trend, indicating that f-$FePSe_3$/CNT has better cycle performance. In particular, although f-FeSe/CNT is steady, the capacity is lower than that of f-$FePSe_3$/CNT, which can be attributed to P inside $FePSe_3$ reacted with K to form K_4P_3. Compared with the rate performances of 2D carbon-treated Se-based anode material and other materials ($FeSe_2$ and FeP) applied to PIBs are shown in Fig. 3f [46,49–55]. First, it can be found that the rate performance of most materials is limited to about 5 A g^{-1}, except for f-$FePSe_3$/CNT and $MoSe_2$@*N*-HCS. Although $MoSe_2$@*N*-HCS maintains capacity at high current density (10 A g^{-1}), it obviously delivers lower capacity than f-$FePSe_3$/CNT. Notably, the capacity of SnSSe/MGS has higher than f-$FePSe_3$/CNT, but the advantage of f-$FePSe_3$/CNT is that it can maintain high capacity at high current density (10 A g^{-1}). In addition, the long-term cycling performance of $FePSe_3$, f-$FePSe_3$, f-$FePSe_3$/CNT, f-FeSe,

and f-FeSe/CNT at 500 mA g^{-1} was also compared (Fig. 3g). The capacity of both of $FePSe_3$ and f-$FePSe_3$ significantly decays to zero although the capacity of f-$FePSe_3$ is higher than that of $FePSe_3$. However, in order to observe the difference between the 1D/2D hybrid or 2D/2D hybrid, the long-term cycling performance of f-$FePSe_3$/graphite at 500 mA g^{-1} was also investigated (Figure S13). The capacity of f-$FePSe_3$/graphite obviously dropped close to zero after 400 cycles, but f-$FePSe_3$/CNT can cycle stably for 1000 cycles and maintain the special capacity of 223.6 mA h g^{-1}. In addition, f-FeSe/CNT can also cycle stably for 1000 cycles and delivers the capacity of 130.7 mA h g^{-1}, but the capacity is lower than that of f-$FePSe_3$/CNT. Based on the above results, CNT can improve the electrochemical performance of 2D materials ($FePSe_3$ and FeSe), indicating that the 3D structure designed in this work is a beneficial method to protect the 2D materials to avoid the

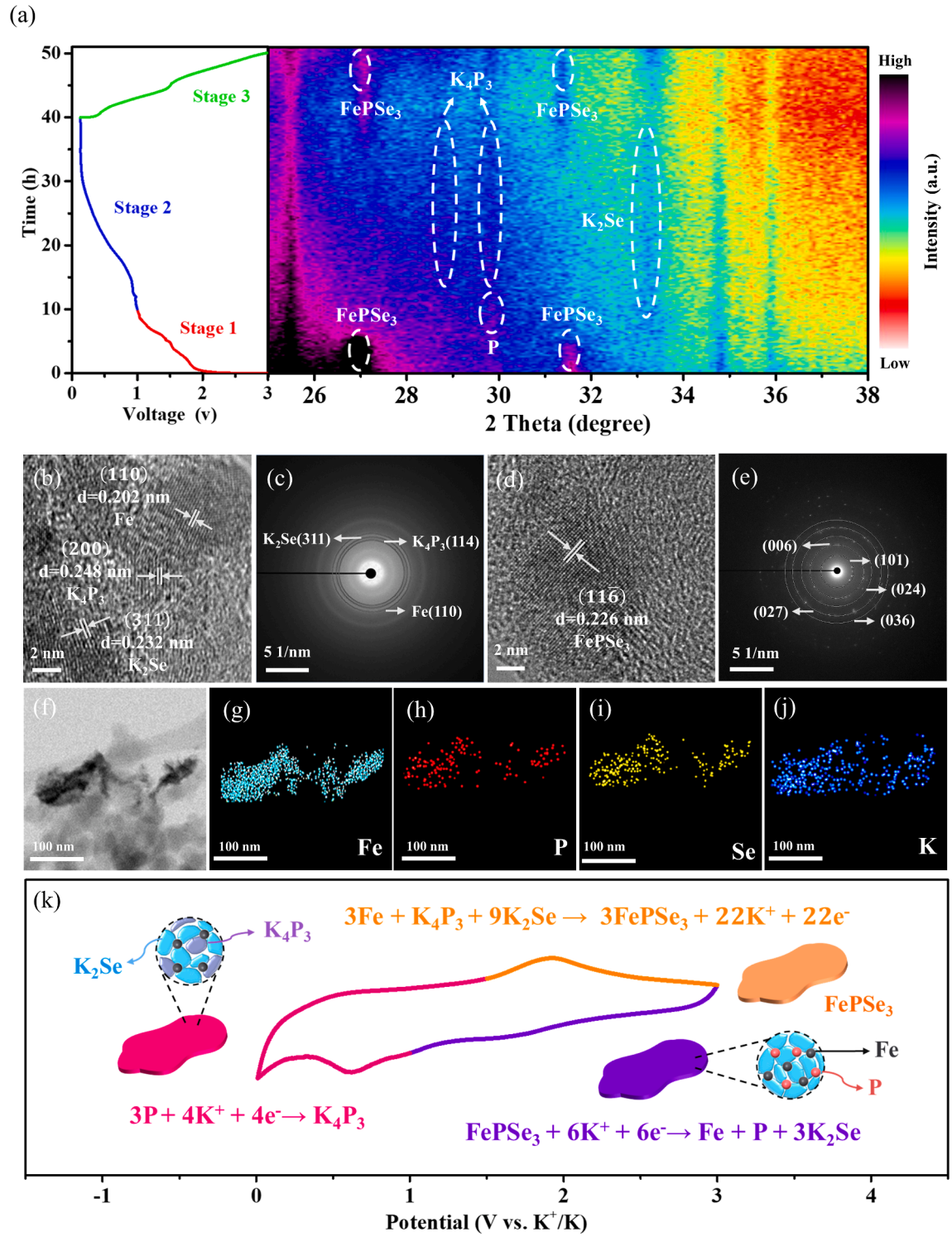

Fig. 4. (a) *In-situ* XRD patterns of the $FePSe_3$ electrode during potassiation/depotassiation process of the initial cycle. HRTEM and SAED images of the $FePSe_3$ electrode after (b, c) discharging to 0.01 V and (d, e) charging to 3.0 V. (f–j) EDS mapping images of the $FePSe_3$ electrode after discharging to 0.01 V. (k) Schematic illustration of the K^+ storage mechanism of $FePSe_3$ during the conversion process.

material fragmentation caused by volume expansion during charging/discharging process. In addition, CV measurements, galvanostatic intermittent titration technique (GITT) tests, *in-situ* electrochemical impedance spectroscopy (EIS) and *ex-situ* EIS measurements were performed to reveal the K^+ storage kinetics (Figures S14-S16). The results show that f-$FePSe_3$/CNT exhibits excellent electrochemical kinetics.

To gain insight into the K^+ storage mechanism of the $FePSe_3$ electrodes, *in-situ* and *ex-situ* XRD of $FePSe_3$ were performed. The *in-situ* XRD patterns of $FePSe_3$ electrodes during the first cycle at 50 mA g^{-1} between 0.01 and 3.0 V (vs K^+/K) are shown in Fig. 4a. During the first discharging process, two strong peaks were initially observed at 26.9° and 31.6°, which belong to the peaks of $FePSe_3$. After discharging to 1.5 V, the peak of $FePSe_3$ disappears, and two peaks appear at 29.8° and 33.1°, which are assigned to P (PDF 04–005-7287) and K_2Se (PDF 04–007-1643), respectively, indicating that the conversion reaction between $FePSe_3$ and K^+ and the formation of P and K_2Se. Then, after further discharging to 1 V, new strong peaks appear at 28.9° and 29.7°, which belong to K_4P_3 (PDF 04–007-1643), indicating that P further reacts with K to form K_4P_3. After charging to 1.8 V, it can be found that the peaks of K_4P_3 and K_2Se disappear, and there are two strong peaks at 26.9° and 31.6°, which are attributed to $FePSe_3$, indicating that the first cycle of charge–discharge reaction is a reversible reaction. However, due to the use of a Be window in *in-situ* XRD, the phase change of Fe cannot be clearly observed. Therefore, through the analysis results of *ex-situ* XRD, it can be observed that there is a weak peak at 44.6°, which can be attributed to Fe (PDF 00–006-0696) after discharging to 1.2 V (Figure S17). With the continuous discharge, the peak of Fe gradually increases, meaning the complete conversion reaction between $FePSe_3$ and K^+ to form Fe、K_4P_3 and K_2Se. The morphology and phase evolution of $FePSe_3$ was investigated at fully discharged state (0.01 V) and fully charged state (3.0 V) by HRTEM and SAED. Fig. 4b shows that the HRTEM image at fully discharged state shows some lattice fringes with lattice spacings of 0.202, 0.248, 0.232 nm, corresponding to the (1 1 0) plane of Fe, the (3 1 1) plane of K_2Se and the (2 0 0) plane of K_4P_3, respectively. Fig. 4c is the corresponding SAED, the d-spacing of the diffraction rings can be assigned to the Fe (1 1 0) plane, K_2Se (3 1 1) plane and K_4P_3 (1 1 4) plane. These results are consistent with *in-situ* and *ex-situ* XRD, indicating the conversion process from $FePSe_3$ to Fe, K_2Se, and K_4P_3 after discharge to 0.01 V. In addition, after fully charged to 3.0 V, the morphology of $FePSe_3$ changes back to layered material, but the size of the layered $FePSe_3$ becomes small due to potassiation (Figure S18). And, it can be observed that $FePSe_3$ in f-$FePSe_3$/CNT is still uniformly dispersed in the CNTs after 5 or 50 cycles, but $FePSe_3$ has a tendency to agglomerate gradually, indicating that 3D structure can prevent f-$FePSe_3$ from agglomerating. The corresponding lattice fringes in Fig. 4d and d-spacing of the diffraction rings in Fig. 4e can be indexed to $FePSe_3$, thus confirming the reversibility of $FePSe_3$ during K^+ storage. From the EDS elemental mapping, it is found that the K, Fe, P, and Se signals show strong intensities, which can be indicated the formation of Fe, K_2Se and K_4P_3 after discharging to 0.01 V (Fig. 4f-j). To understand the conversion mechanism of $FePSe_3$, *ex-situ* XPS study of Fe, P, and Se elements was performed on electrodes at different discharge states (Figure S19). The spectrum of Fe 2p on the pristine electrode shows the main four peaks Fe^{2+} $2p_{3/2}$ (710.4 eV), Fe^{2+} $2p_{1/2}$ (722.5 eV), Fe^{3+} $2p_{3/2}$ (713.4 eV) and Fe^{3+} $2p_{1/2}$ (726.3 eV). After discharging to 1 V, the peaks of Fe^0 $2p_{3/2}$ (707.5 eV) and Fe^0 $2p_{1/2}$ (720.2 eV) emerge, which are related to the metallic Fe phase. Fe^0 $2p_{3/2}$ and Fe^0 $2p_{1/2}$ can also be observed after discharged to 0.01 V. In the P 2p spectrum, the pristine electrode shows the typical P $2p_{3/2}$ (132.4 eV) and P $2p_{1/2}$ (133.5 eV) features, which is consistent with the XPS results in Fig. 2g. From open circuit potential (OCP) to 0.01 V, it can be found that the main peak gradually shifts to lower binding energy due to the formation of K_4P_3. In the Se 2p spectrum, it can be clearly observed that the main peak shifts to lower binding energies from OCP to 0.01 V, which can be attributed to the formation of K_2Se. This result is highly consistent with the XRD analysis result. In summary, through the results of *in-situ* and *ex-situ* XRD, *ex-situ* TEM, and *ex-situ* XPS, the reaction mechanism of $FePSe_3$ shown by the schematic diagram in Fig. 4k is inferred, the corresponding reaction equation for the conversion reaction of potassiation/depotassiation is described as follows:

Stage I: $FePSe_3 + 6\ K^+ + 6e^- \rightarrow Fe + P + 3K_2Se$.
Stage II: $3P + 4\ K^+ + 4e^- \rightarrow K_4P_3$.
Stage III: $K_4P_3 + 9K_2Se + 3Fe \rightarrow 3FePSe_3 + 22\ K^+ + 22e^-$.

To further investigate why f-$FePSe_3$/CNT electrode has excellent electrochemical performance compared to $FePSe_3$ electrode and f-$FePSe_3$ electrode, DFT calculations were performed to study migration mechanism for potassium ions on the surface of f-$FePSe_3$, between $FePSe_3$ layers, and between f-$FePSe_3$ and CNT. Fig. 5a-g show the possible diffusion paths and corresponding migration energy barriers for $FePSe_3$, f-$FePSe_3$, and f-$FePSe_3$/CNT. The energy barrier can estimate the energy demand of alkali metal atoms to transport through the electrode. Therefore, the electrode materials with lower energy diffusion barriers will experience fast alkali metal atomic transport and storage, resulting in better electrochemical performance. Although the migration energy (0.11 eV) of f-$FePSe_3$ is lower than that of $FePSe_3$ (0.46 eV), indicating that exfoliation strategy can improve the electrochemical performance of $FePSe_3$. However, the calculated migration energies of f-$FePSe_3$/CNT at each site are significantly lower than those of f-$FePSe_3$, indicating that the f-$FePSe_3$/CNT has faster potassium ion diffusion than f-$FePSe_3$. 1D/2D hybrid promotes charge transfer and ion transport during the electrochemical reaction, leading to the excellent kinetic and rate performance. These results are consistent with the electrochemical test results. The f-$FePSe_3$/CNT can deliver a special capacity of 124.9 mA h g^{-1} at high density (10.0 A g^{-1}). Conversely, the capacity of $FePSe_3$ and f-$FePSe_3$ approached zero at 6.0 A g^{-1}. In addition, in the test of rate capability and cycling stability, FeSe group has lower capacity compared with $FePSe_3$ group, which can be attributed to the slower potassium ion diffusion kinetics of FeSe. It is worth noting that the advantages of 1D/2D hybrids can also be observed in the group of FeSe. Compared with f-FeSe, f-FeSe/CNT exhibits excellent rate capability and long-cycle stability. Interestingly, it is found that the morphology of f-$FePSe_3$/CNT after 5 cycles is still similar to the first circle in the process of mechanism analysis, indicating that 1D CNTs effectively prevent $FePSe_3$ agglomeration. Conversely, the agglomeration problems produce on the $FePSe_3$ electrode after 5 cycle. Based on the analysis of electrochemical performance, mechanism and DFT results, Fig. 5h shows that the 1D/2D hybrid is beneficial to accelerate the charge transfer rate of 2D materials and promote ion diffusion because the 1D CNTs tightly wrap around the 2D $FePSe_3$. This material design approach offers mutually beneficial impacts as the restacking of $FePSe_3$ can be prevented and the aggregation of CNTs can be suppressed. Furthermore, the 1D CNTs help to maintain a larger K ion spacing to penetrate between 2D $FePSe_3$ layers, thus facilitating the storage of more K ions. Therefore, it can be speculated that f-$FePSe_3$/CNT is a promising anode material, and the feasibility of assembling with other cathode materials into two systems, potassium-ion batteries (PIBs) and potassium-ion hybrid capacitors (PIHCs), can be further investigated.

Based on the excellent performance of the half-cell, a K-ion full cell (referred to as f-$FePSe_3$/CNT//PB) was assembled using f-$FePSe_3$/CNT as anode and PB as cathode (Fig. 6). Before assembling K-ion full cell, the XRD pattern and electrochemical properties of PB were investigated (Figure S20). The results demonstrate that PB was successfully synthesized and excellent electrochemical performance as a cathode. The first charge/discharge curves of f-$FePSe_3$/CNT half-cell, PB half-cell and f-$FePSe_3$/CNT//PB full-cell at 0.10 A g^{-1} are shown in Fig. 6b. According to the charge–discharge curve, the working voltage of f-$FePSe_3$/CNT//PB full-cell ranges from 1 to 3.8 V. The mass ratio of anode and cathode is set to 1:4.5. Figure S21 shows the CV curves of f-$FePSe_3$/CNT//PB under 1 mV s^{-1}. The overlapping peaks in the CV curves indicate that the f-$FePSe_3$/CNT//PB full cell is in the proper voltage window of 1.0–3.8 V.

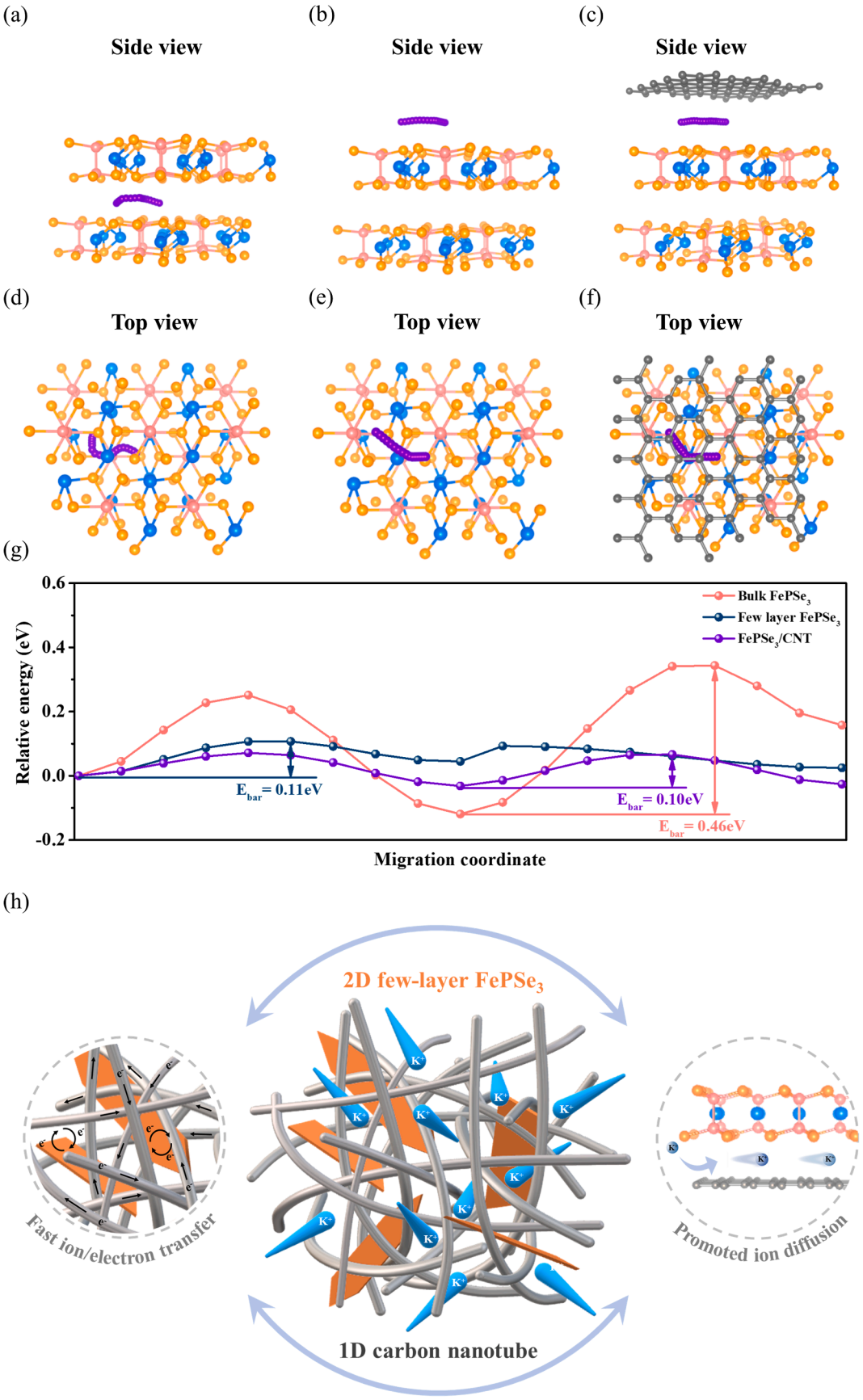

Fig. 5. The (a-c) side and (d-f) top view of potassium diffusion pathways on the surface of f-$FePSe_3$, between $FePSe_3$ layers, and between f-$FePSe_3$ and CNT. (g) Calculated energy barriers of K on the surface of f-$FePSe_3$, between $FePSe_3$ layers, and between f-$FePSe_3$ and CNT. (h) Schematic illustration of advantages of 2D f-$FePSe_3$/1D CNT hybrid for PIB.

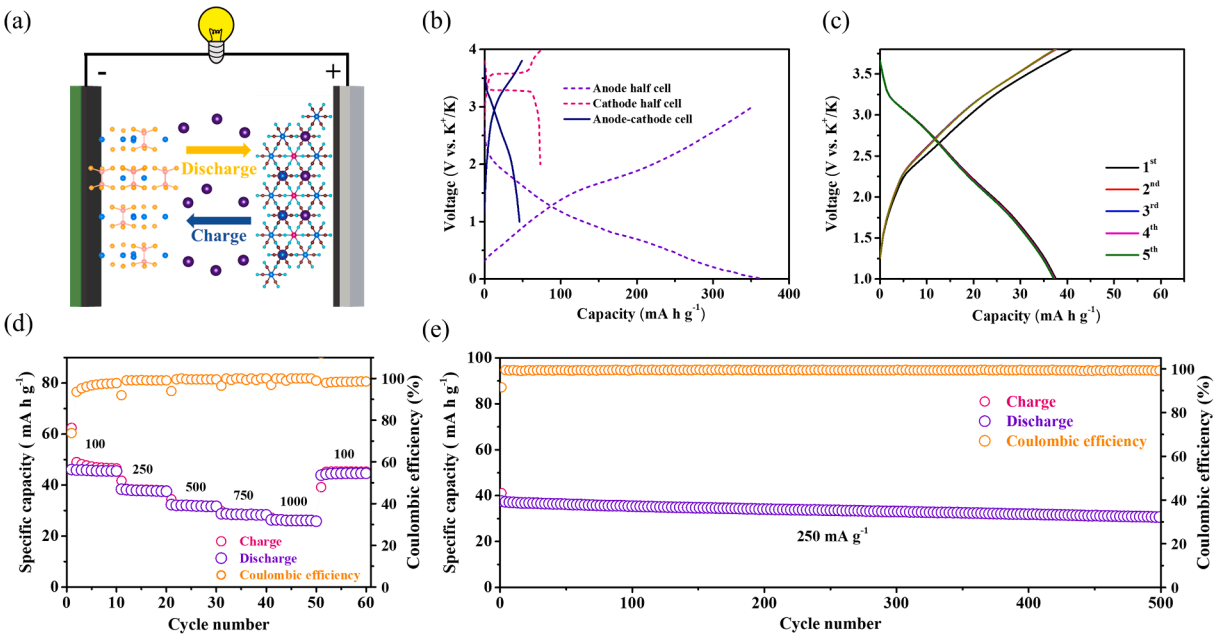

Fig. 6. (a) Schematic diagram of a f-FePSe$_3$/CNT//PB full cell. (b) Charge/discharge curves of PB and f-FePSe$_3$/CNT half cells and a f-FePSe$_3$/CNT//PB full cell. (c) Charge/discharge profiles at 50 mA g^{-1}. (d) Rate performance at current densities ranging from 0.1 to 1 A/g. (e) Long-term cycling performance at 250 mA g^{-1}.

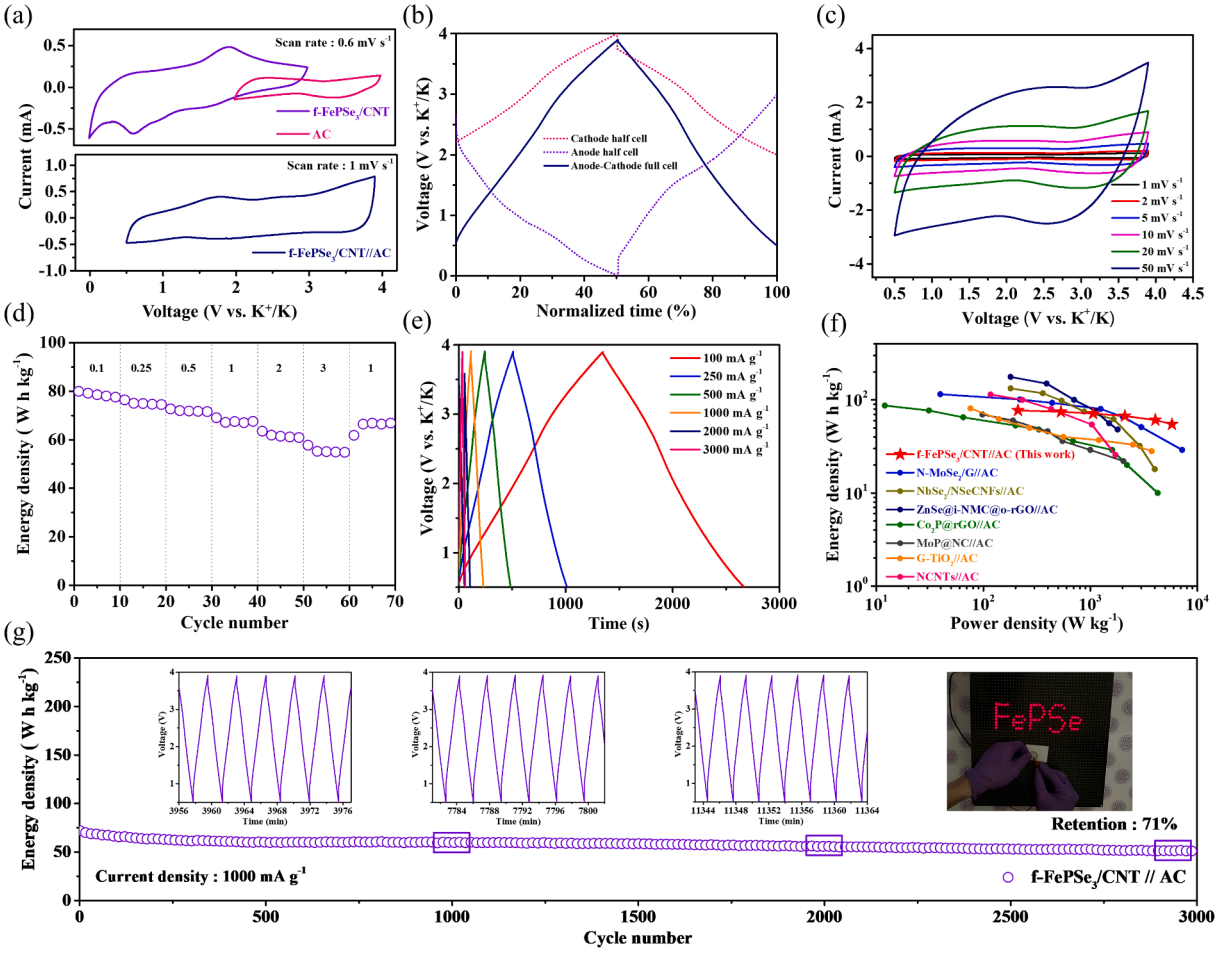

Fig. 7. (a) CV profiles of AC and f-FePSe$_3$/CNT half cells (top) and a f-FePSe$_3$/CNT//AC PIHC (bottom). (b) Normalized charge/discharge curves of two half cells and a full cell. (c) CV profiles at various current densities. (d) Rate performance at various current densities from 0.1 to 3 A/g. (e) Charge/discharge profiles at different current densities. (f) Ragone plots of the f-FePSe$_3$/CNT//AC PIHC compared with previously reported PIHCs. (g) Long-term cycling performance at 1 A g^{-1}. Insets of (g) present the pseudocapacitive profile and a digital picture while lighting a LED bulb.

The charge/discharge curves of the f-$FePSe_3$/CNT//PB full cell show the initial charge and discharge capacity are 62.4 and 46.1 mA h g^{-1}. Fig. 6c shows the charge–discharge curves of the first five cycles of the f-$FePSe_3$/CNT//PB full cell. The overlapping shapes during cycling indicate that the f-$FePSe_3$/CNT//PB full cells have good reversibility and stability. In Fig. 6d, the rate performance of f-$FePSe_3$/CNT//PB shows that the discharge capacities are 45.5, 37.5, 31.6, 28.3 and 25.8 mA h g^{-1} at the current densities of 0.1, 0.25, 0.5, 0.75 and 1 A g^{-1}, respectively. The results demonstrate the high rate capability of the full cell. Fig. 6e shows the cycle stability test of the full cell at a current density of 0.25 A g^{-1}. After 500 cycles, the f-$FePSe_3$/CNT//PB full-cell retains 81.3 % of the initial capacity with an average CE of about 99.4 %. Therefore, the excellent electrochemical performances of f-$FePSe_3$/CNT demonstrate its potential as a high-performance anode material for PIB.

Considering the high reaction kinetics and potassium storage capacity of the as-synthesized f-$FePSe_3$/CNT anode, a PIHC device (labeled as f-$FePSe_3$/CNT//AC) was prepared with AC cathode. Before assembling PIHCs, the electrochemical properties of AC were investigated, including charge and discharge curves, cycling performance and rate performance (Figure S22), which demonstrated excellent electrochemical performance as a cathode for PIHCs. The optimal mass ratio of cathode and anode of 1:1 was selected for maximum output power. To select the working window of f-$FePSe_3$/CNT //AC PIHC, the voltage range of f-$FePSe_3$/CNT anode and AC cathode in half-cell configuration was investigated (Fig. 7a and b). Optimally, the potential window of full cell was set between 0.5 and 3.9 V. In addition, the kinetics analysis of f-$FePSe_3$/CNT//AC was also carried out by CV measurement at different scan rates in the potential range from 0.5 to 3.9 V (Fig. 7c). The results show that CV curves exhibit quasi-rectangular shapes without polarization and it can be operated steadily in a high voltage window, indicating that the pseudocapacitive in f-$FePSe_3$/CNT//AC PIHC is highly dominated. As shown in Fig. 7d, f-$FePSe_3$/CNT//AC exhibits an ultrahigh energy density of 77.3 Wh kg^{-1} at 0.1 A g^{-1}, even it can still deliver 54.7 Wh kg^{-1} at 3 A g^{-1}. The excellent rate capability of PIHCs is due to the fast kinetics of the electrode material. The discharge/charge curves at different current densities are almost straight, indicating the K^+ storage mechanism mainly controlled by the capacitive behavior (Fig. 7e). The Ragone plots in terms of the energy/power density of various PIHC systems are shown in Fig. 7f. The f-$FePSe_3$/CNT//AC PIHC delivers an energy density of 77.3 Wh kg^{-1} at a power density of 210.5 W kg^{-1}. Even at a high power density of 5790.8 W kg^{-1}, the f-$FePSe_3$/CNT//AC PIHC can achieve energy density of 54.7 Wh kg^{-1}, indicating that f-$FePSe_3$/CNT//AC PIHC can deliver high energy and high power simultaneously. Also, it can be observed that it exhibits better power/energy density compared with the previously reported PIHC. For example, N-$MoSe_2$/G//AC [56], $NbSe_2$/NSeCNFs//AC [57], ZnSe@i-NMC@o-rGO//AC [58], Co_2P@//AC [59], MoP@NC//AC [60]; G-TiO//AC [61] and NCNTs//AC [62], etc. Considering the cycle stability, the f-$FePSe_3$/CNT//AC exhibits energy density of 51.4 Wh kg^{-1} with a capacity retention of 71 % after 3000 cycles at 1 A g^{-1} (Fig. 7g). In addition, $FePSe_3$//AC can easily light up 81 red LED (see the inset in Fig. 7g), thus demonstrating its application potential. This study may introduce a new application area for ternary metal phosphorus trichalcogenides and provide an alternative material for further development of high-performance PIHCs.

4. Conclusion

In conclusion, an architectural 3D f-$FePSe_3$/CNT hybrid structure is proposed, in which 1D CNTs are tightly wound around f-$FePSe_3$ crystals, for use as an excellent anode electrode for PIBs. Due to the synergistic effect, 2D $FePSe_3$ contributes highly surface-controlled capacitive storage through the 1D CNT network, and the electrochemical affinity for K ions is significantly enhanced. On the other hand, the 1D/2D hybrids can prevent the 2D material from agglomerating again during the charging and discharging process, thereby improving the electrochemical performance of the material. Moreover, we also demonstrate that the f-$FePSe_3$/CNT anode exhibits superior K storage performance compared to the f-FeSe/CNT anodes due to the following advantages: (i) the addition of P atoms makes $FePSe_3$ theoretical capacity higher than FeSe; (ii) f-$FePSe_3$/CNT electronic conductivity is higher than f-FeSe/CNT; (iii) The low diffusion barrier of f-$FePSe_3$ relative to f-FeSe facilitates fast ion diffusion and electrochemical reaction kinetics. Therefore, this work provides a feasible and scalable electrode design strategy for the practical application of layered compound-based potassium ion storage devices with high energy density and power density.

CRediT authorship contribution statement

Yan-Fu Huang: Conceptualization, Methodology, Data curation. **Yi-Chun Yang:** Methodology, Data curation. **Hsing-Yu Tuan:** Conceptualization, Resources, Supervision, Writing – review & editing.

Declaration of Competing Interest

The authors declare that they have no known competing financial interests or personal relationships that could have appeared to influence the work reported in this paper.

Data availability

No data was used for the research described in the article.

Acknowledgements

This work was supported by the financial support from the 2030 Cross-Generation Young Scholars Program by Ministry of Science and Technology, Taiwan (MOST 111-2628-E-007-008). H.-Y. Tuan also acknowledges the financial support of National Tsing Hua University, Taiwan, through the grant of 111QI030E1.

Appendix A. Supplementary data

Supplementary data to this article can be found online at https://doi.org/10.1016/j.cej.2022.139013.

References

[1] W. Zhang, J. Mao, S. Li, Z. Chen, Z. Guo, Phosphorus-based alloy materials for advanced potassium-ion battery anode, J. Am. Chem. Soc. 139 (9) (2017) 3316–3319.
[2] J. Wu, S. Liu, Y. Rehman, T. Huang, J. Zhao, Q. Gu, J. Mao, Z. Guo, Phase Engineering of Nickel Sulfides to Boost Sodium-and Potassium-Ion Storage Performance, Adv. Funct. Mater. 31 (2021) 2010832.
[3] X. Yuan, B. Zhu, J. Feng, C. Wang, X. Cai, R. Qin, Recent advance of biomass-derived carbon as anode for sustainable potassium ion battery, Chem. Eng. J. 405 (2021), 126897.
[4] C. Yang, J. Feng, F. Lv, J. Zhou, C. Lin, K. Wang, Y. Zhang, Y. Yang, W. Wang, J. Li, Metallic graphene-like VSe_2 ultrathin nanosheets: superior potassium-ion storage and their working mechanism, Adv. Mater. 30 (2018) 1800036.
[5] J. Chu, Q. Yu, K. Han, L. Xing, C. Gu, Y. Li, Y. Bao, W.(Wang, Yolk–shell structured FeS/MoS_2@ nitrogen-doped carbon nanocubes with sufficient internal void space as an ultrastable anode for potassium-ion batteries, J. Mater. Chem. A 8 (45) (2020) 23983–23993.
[6] K.-T. Chen, H.-Y. Tuan, Bi–Sb nanocrystals embedded in phosphorus as high-performance potassium ion battery electrodes, ACS nano 14 (9) (2020) 11648–11661.
[7] Y. Wu, H. Zhao, Z. Wu, L. Yue, J. Liang, Q. Liu, Y. Luo, S. Gao, S. Lu, G. Chen, X. Shi, B. Zhong, X. Guo, X. Sun, Rational design of carbon materials as anodes for potassium-ion batteries, Energy Stor. Mater. 34 (2021) 483–507.
[8] Y. Xu, C. Zhang, M. Zhou, Q. Fu, C. Zhao, M. Wu, Y. Lei, Highly nitrogen doped carbon nanofibers with superior rate capability and cyclability for potassium ion batteries, Nat. Commun. 9 (2018) 1–11.
[9] C.-Y. Tsai, C.-H. Chang, T.-L. Kao, K.-T. Chen, H.-Y. Tuan, Shape matters: $SnP_{0.94}$ teardrop nanorods with boosted performance for potassium ion storage, Chem. Eng. J. 417 (2021), 128552.
[10] Y. An, Y. Tian, L. Ci, S. Xiong, J. Feng, Y. Qian, Micron-sized nanoporous antimony with tunable porosity for high-performance potassium-ion batteries, ACS nano 12 (12) (2018) 12932–12940.

[11] Y. Yang, H. Hou, G. Zou, W. Shi, H. Shuai, J. Li, X. Ji, Electrochemical exfoliation of graphene-like two-dimensional nanomaterials, Nanoscale 11 (1) (2019) 16–33.

[12] J.N. Coleman, M. Lotya, A. O'Neill, S.D. Bergin, P.J. King, U. Khan, K. Young, A. Gaucher, S. De, R.J. Smith, I.V. Shvets, S.K. Arora, G. Stanton, H.-Y. Kim, K. Lee, G.T. Kim, G.S. Duesberg, T. Hallam, J.J. Boland, J.J. Wang, J.F. Donegan, J. C. Grunlan, G. Moriarty, A. Shmeliov, R.J. Nicholls, J.M. Perkins, E.M. Grieveson, K. Theuwissen, D.W. McComb, P.D. Nellist, V. Nicolosi, Two-dimensional nanosheets produced by liquid exfoliation of layered materials, Science 331 (6017) (2011) 568–571.

[13] S. Ahmed, J. Yi, Two-dimensional transition metal dichalcogenides and their charge carrier mobilities in field-effect transistors, Nano-Micro Lett. 9 (2017) 1–23.

[14] L. Peng, Y. Zhu, D. Chen, R.S. Ruoff, G. Yu, Two-dimensional materials for beyond-lithium-ion batteries, Adv. Energy Mater. 6 (2016) 1600025.

[15] Y. Xue, Q. Zhang, W. Wang, H. Cao, Q. Yang, L. Fu, Opening two-dimensional materials for energy conversion and storage: a concept, Adv. Energy Mater. 7 (19) (2017) 1602684.

[16] M.S. Stark, K.L. Kuntz, S.J. Martens, S.C. Warren, Intercalation of layered materials from bulk to 2D, Adv. Mater. 31 (2019) 1808213.

[17] J. Wan, S.D. Lacey, J. Dai, W. Bao, M.S. Fuhrer, L. Hu, Tuning two-dimensional nanomaterials by intercalation: materials, properties and applications, Chem. Soc. Rev. 45 (2016) 6742–6765.

[18] K. Share, A.P. Cohn, R. Carter, B. Rogers, C.L. Pint, Role of nitrogen-doped graphene for improved high-capacity potassium ion battery anodes, ACS nano 10 (10) (2016) 9738–9744.

[19] P. Lian, Y. Dong, Z.-S. Wu, S. Zheng, X. Wang, S. Wang, C. Sun, J. Qin, X. Shi, X. Bao, Alkalized Ti_3C_2 MXene nanoribbons with expanded interlayer spacing for high-capacity sodium and potassium ion batteries, Nano Energy 40 (2017) 1–8.

[20] B. Jia, Q. Yu, Y. Zhao, M. Qin, W. Wang, Z. Liu, C.Y. Lao, Y. Liu, H. Wu, Z. Zhang, Bamboo-like hollow tubes with MoS_2/N-doped-C interfaces boost potassium-ion storage, Adv. Funct. Mater. 28 (2018) 1803409.

[21] L. Fang, J. Xu, S. Sun, B. Lin, Q. Guo, D. Luo, H. Xia, Few-layered tin sulfide nanosheets supported on reduced graphene oxide as a high-performance anode for potassium-ion batteries, Small 15 (2019) 1804806.

[22] L. Xing, K. Han, Q. Liu, Z. Liu, J. Chu, L. Zhang, X. Ma, Y. Bao, P. Li, W.A. Wang, Hierarchical two-atom-layered WSe_2/C ultrathin crumpled nanosheets assemblies: engineering the interlayer spacing boosts potassium-ion storage, Energy Stor. Mater. 36 (2021) 309–317.

[23] R. Gusmão, Z. Sofer, M. Pumera, Metal phosphorous trichalcogenides ($MPCh_3$): from synthesis to contemporary energy challenges, Angew. Chem. Int. Ed. 58 (2019) 9326–9337.

[24] F. Wang, T.A. Shifa, P. Yu, P. He, Y. Liu, F. Wang, Z. Wang, X. Zhan, X. Lou, F. Xia, New frontiers on van der Waals layered metal phosphorous trichalcogenides, Adv. Funct. Mater. 28 (2018) 1802151.

[25] X. Yang, Y. Luo, J. Li, H. Wang, Y. Song, J. Li, Z. Guo, Tuning Mixed Electronic/Ionic Conductivity of 2D $CdPS_3$ Nanosheets as an Anode Material by Synergistic Intercalation and Vacancy Engineering, Adv. Funct. Mater. 32 (2022) 2112169.

[26] Y. Feng, M. Xu, T. He, B. Chen, F. Gu, L. Zu, R. Meng, J. Yang, CoPSe: A New Ternary Anode Material for Stable and High-Rate Sodium/Potassium-Ion Batteries, Adv. Mater. 33 (2021) 2007262.

[27] R. Samal, G. Sanyal, B. Chakraborty, C.S. Rout, Two-dimensional transition metal phosphorous trichalcogenides (MPX_3): a review on emerging trends, current state and future perspectives, J. Mater. Chem. A 9 (2021) 2560–2591.

[28] Y. Ma, X. Lian, N. Xu, H. Jiang, L. Li, D. Zhang, G. Hu, S. Peng, Rational design of few-layer $FePS_3$ nanosheets@ N-doped carbon composites as anodes for sodium-ion batteries, Chem. Eng. J. 427 (2022), 130882.

[29] H. Li, G. Lu, Y. Wang, Z. Yin, C. Cong, Q. He, L.u. Wang, F. Ding, T. Yu, H. Zhang, Mechanical Exfoliation and Characterization of Single- and Few-Layer Nanosheets of WSe_2, TaS_2, and $TaSe_2$, Small 9 (11) (2013) 1974–1981.

[30] K.F. Mak, C. Lee, J. Hone, J. Shan, T.F. Heinz, Atomically thin MoS_2: a new direct-gap semiconductor, Phys. Rev. Lett. 105 (2010), 136805.

[31] C. Ataca, H. Şahin, S. Ciraci, Stable, single-layer MX_2 transition-metal oxides and dichalcogenides in a honeycomb-like structure, J. Phys. Chem. C 116 (16) (2012) 8983–8999.

[32] Y. Hao, A. Huang, S. Han, H. Huang, J. Song, X. Sun, Z. Wang, L. Li, F. Hu, J. Xue, Plasma-treated ultrathin ternary $FePSe_3$ nanosheets as a bifunctional electrocatalyst for efficient zinc–air batteries, ACS Appl. Mater. Interfaces 12 (2020) 29393–29403.

[33] Y. Sang, L. Wang, X. Cao, G. Ding, Y. Ding, Y. Hao, N. Xu, H. Yu, L. Li, S. Peng, Emerging 2D-Layered $MnPS_3$/rGO composite as a superior anode for sodium-ion batteries, J. Alloys Compd. 831 (2020), 154775.

[34] D. Adekoya, S. Zhang, M. Hankel, 1D/2D C_3N_4/graphene composite as a preferred anode material for lithium ion batteries: importance of heterostructure design via DFT computation, ACS Appl. Mater. Interfaces 12 (23) (2020) 25875–25883.

[35] Z. He, J. Zhang, X. Li, S. Guan, M. Dai, S. Wang, 1D/2D Heterostructured photocatalysts: From design and unique properties to their environmental applications, Small 16 (2020) 2005051.

[36] Z.-M. Dang, M.-S. Zheng, J.-W. Zha, 1D/2D carbon nanomaterial-polymer dielectric composites with high permittivity for power energy storage applications, Small 12 (13) (2016) 1688–1701.

[37] X. Sun, Y. Pu, F. Wu, J. He, G. Deng, Z. Song, X. Liu, J. Shui, R. Yu, 0D–1D-2D multidimensionally assembled Co_9S_8/CNTs/MoS_2 composites for ultralight and broadband electromagnetic wave absorption, Chem. Eng. J. 423 (2021), 130132.

[38] Z. Ye, Y. Jiang, L. Li, F. Wu, R. Chen, Enhanced catalytic conversion of polysulfide using 1D CoTe and 2D MXene for heat-resistant and lean-electrolyte Li–S batteries, Chem. Eng. J. 430 (2022), 132734.

[39] J. Luo, X. Lu, E. Matios, C. Wang, H. Wang, Y. Zhang, X. Hu, W. Li, Tunable MXene-derived 1D/2D hybrid nanoarchitectures as a stable matrix for dendrite-free and ultrahigh capacity sodium metal anode, Nano Lett. 20 (10) (2020) 7700–7708.

[40] D. Mukherjee, S. Sampath, Few-layer iron selenophosphate, $FePSe_3$: efficient electrocatalyst toward water splitting and oxygen reduction reactions, ACS Appl. Energy Mater. 1 (2017) 220–231.

[41] L. Chen, X. Yang, X. Fu, C. Wang, C. Liang, M. Wu, Facile Solvothermal Synthesis of Uniform Iron Selenide Nanoplates, Eur. J. Inorg. Chem. 2011 (13) (2011) 2098–2102.

[42] J.-K. Meng, W.-W. Wang, Q.-C. Wang, M.-H. Cao, Z.-W. Fu, X.-J. Wu, Y.-N. Zhou, Graphene supported ultrafine tin oxide nanoparticles enable conversion reaction dominated mechanism for sodium-ion batteries, Electrochim. Acta 303 (2019) 32–39.

[43] K.-T. Chen, S. Chong, L. Yuan, Y.-C. Yang, H.-Y. Tuan, Conversion-alloying dual mechanism anode: Nitrogen-doped carbon-coated Bi_2Se_3 wrapped with graphene for superior potassium-ion storage, Energy Stor. Mater. 39 (2021) 239–249.

[44] C. He, S. Wu, N. Zhao, C. Shi, E. Liu, J. Li, Carbon-encapsulated Fe_3O_4 nanoparticles as a high-rate lithium ion battery anode material, ACS nano 7 (5) (2013) 4459–4469.

[45] J. Tang, C.-Y. Wang, F. Xiu, A.J. Hong, S. Chen, M. Wang, C. Zeng, H.-J. Yang, H.-Y. Tuan, C.-J. Tsai, Single-crystalline Ni_2Ge/Ge/Ni_2Ge nanowire heterostructure transistors, Nanotechnology 21 (2010), 505704.

[46] Z. Yi, J. Xu, Z. Xu, M. Zhang, Y. He, J. Bao, X. Zhou, Ultrafine SnSSe/multilayer graphene nanosheet nanocomposite as a high-performance anode material for potassium-ion half/full batteries, J. Energy Chem. 60 (2021) 241–248.

[47] S.-C. Lu, M.-C. Hsiao, M. Yorulmaz, L.-Y. Wang, P.-Y. Yang, S. Link, W.-S. Chang, H.-Y. Tuan, Single-crystalline copper nano-octahedra, Chem. Mater. 27 (24) (2015) 8185–8188.

[48] T. Li, Y. Wang, L. Yuan, Q. Zhou, S. Qiao, Z. Liu, S. Chong, An α-MnSe nanorod as anode for superior potassium-ion storage via synergistic effects of physical encapsulation and chemical bonding, Chem. Eng. J. 446 (2022) 137152.

[49] L. Xu, W. Guo, L. Zeng, X. Xia, Y. Wang, P. Xiong, Q. Chen, J. Zhang, M. Wei, Q. Qian, V_3Se_4 embedded within N/P co-doped carbon fibers for sodium/potassium ion batteries, Chem. Eng. J. 419 (2021), 129607.

[50] M. Cai, H. Zhang, Y. Zhang, B. Xiao, L. Wang, M. Li, Y. Wu, B. Sa, H. Liao, L. i. Zhang, S. Chen, D.-L. Peng, M.-S. Wang, Q. Zhang, Boosting the potassium-ion storage performance enabled by engineering of hierarchical MoSSe nanosheets modified with carbon on porous carbon sphere, Sci. Bull. 67 (9) (2022) 933–945.

[51] F. Zhong, A. Xu, Q.i. Zeng, Y. Wang, G. Li, Z. Xu, Y. Yan, S. Wu, Confining $MoSe_2$ Nanosheets into N-Doped Hollow Porous Carbon Microspheres for Fast-Charged and Long-Life Potassium-Ion Storage, ACS Appl. Mater. Interfaces 13 (50) (2021) 59882–59891.

[52] J. Ge, B. Wang, J. Wang, Q. Zhang, B. Lu, Nature of $FeSe_2$/N-C anode for high performance potassium ion hybrid capacitor, Adv. Energy Mater. 10 (2020) 1903277.

[53] X. Chen, H. Muheiyati, X. Sun, P. Zhou, P. Wang, X. Ding, Y. Qian, L. Xu, Rational Design of Tungsten Selenide@ N-Doped Carbon Nanotube for High-Stable Potassium-Ion Batteries, Small 18 (2022) 2104363.

[54] Q. Tan, K. Han, W. Zhao, P. Li, Z. Liu, S. Li, X. Qu, Synchronous nesting of hollow FeP nanospheres into a three-dimensional porous carbon scaffold via a salt-template method for performance-enhanced potassium-ion storage, Sustain, Energy Fuels 5 (3) (2021) 844–854.

[55] C. Yang, F. Lv, K. Dong, F. Lai, K. Zhao, F.u. Sun, S. Dou, Q. Wang, J. Xu, P. Zhang, T. Arlt, X. Chen, Y. Chen, I. Manke, S. Guo, Carbon-coated ultrathin metallic V_5Se_8 nanosheet for high-energy-density and robust potassium storage, Energy Stor. Mater. 35 (2021) 1–11.

[56] Y. Yi, Z. Sun, C. Li, Z. Tian, C. Lu, Y. Shao, J. Li, J. Sun, Z. Liu, Designing 3D biomorphic nitrogen-doped $MoSe_2$/graphene composites toward high-performance potassium-ion capacitors, Adv. Funct. Mater. 30 (2020) 1903878.

[57] M. Chen, L. Wang, X. Sheng, T. Wang, J. Zhou, S. Li, X. Shen, M. Zhang, Q. Zhang, X. Yu, An ultrastable nonaqueous potassium-ion hybrid capacitor, Adv. Funct. Mater. 30 (2020) 2004247.

[58] J. Ruan, J. Zang, J. Hu, R. Che, F. Fang, F. Wang, Y. Song, D. Sun, Respective Roles of Inner and Outer Carbon in Boosting the K^+ Storage Performance of Dual-Carbon-Confined ZnSe, Adv. Sci. 9 (2022) 2104822.

[59] Y. Wang, Z. Zhang, G. Wang, X. Yang, Y. Sui, F. Du, B.o. Zou, Ultrafine Co_2P nanorods wrapped by graphene enable a long cycle life performance for a hybrid potassium-ion capacitor, Nanoscale Horiz. 4 (6) (2019) 1394–1401.

[60] W. Zong, N. Chui, Z. Tian, Y. Li, C. Yang, D. Rao, W. Wang, J. Huang, J. Wang, F. Lai, Ultrafine MoP nanoparticle splotched nitrogen-doped carbon nanosheets enabling high-performance 3D-printed potassium-ion hybrid capacitors, Adv. Sci. 8 (2021) 2004142.

[61] J. Cai, R. Cai, Z. Sun, X. Wang, N. Wei, F. Xu, Y. Shao, P. Gao, S. Dou, J. Sun, Confining TiO_2 nanotubes in pecvd-enabled graphene capsules toward ultrafast K-Ion storage: in situ TEM/XRD study and DFT analysis, Nano-Micro Lett. 12 (2020) 1–14.

[62] X. Li, M. Chen, L. Wang, H. Xu, J. Zhong, M. Zhang, Y. Wang, Q. Zhang, L. Mei, T. Wang, J. Zhu, B. Lu, X. Duan, Nitrogen-doped carbon nanotubes as an anode for a highly robust potassium-ion hybrid capacitor, Nanoscale Horiz. 5 (12) (2020) 1586–1595.